Monthly Notices
of the
ROYAL ASTRONOMICAL SOCIETY

MNRAS **484,** 2711–2724 (2019)
Advance Access publication 2019 January 16

doi:10.1093/mnras/stz160

The white dwarf mass–radius relation and its dependence on the hydrogen envelope

Alejandra D. Romero,[1★] S. O. Kepler,[1] S. R. G. Joyce,[2] G. R. Lauffer[1] and A. H. Córsico[3,4]

[1] *Physics Institute, Universidade Federal do Rio Grande do Sul, Av. Bento Gonçalves 9500, Brazil*
[2] *Deptartment of Physics & Astronomy, University of Leicester, University Road, Leicester, LE1 7RH, UK*
[3] *Facultad de Ciencias Astronómicas y Geofísicas, Universidad Nacional de La Plata, La Plata 1900, Argentina*
[4] *CONICET, Consejo Nacional de Investigaciones Científcas y Técnicas, Godoy Cruz 2290, Argentina*

Accepted 2019 January 11. Received 2019 January 11; in original form 2018 October 23

Downloaded from https://academic.oup.com/mnras/article-abstract/484/2/2711/5289881 by Iowa State University user on 05 February 2019

ABSTRACT

We present a study of the dependence of the mass–radius relation for DA white dwarf stars on the hydrogen envelope mass and the impact on the value of log g, and thus the determination of the stellar mass. We employ a set of full evolutionary carbon–oxygen core white dwarf sequences with white dwarf mass between 0.493 and 1.05 $\mathrm{M}_{\odot}$. Computations of the pre-white-dwarf evolution uncovers an intrinsic dependence of the maximum mass of the hydrogen envelope on the stellar mass; i.e. it decreases when the total mass increases. We find that a reduction of the hydrogen envelope mass can lead to a reduction in the radius of the model of up to ∼12 per cent. This translates directly to an increase in log g for a fixed stellar mass, which can reach up to 0.11 dex, mainly overestimating the determinations of stellar mass from atmospheric parameters. Finally, we find a good agreement between the results from the theoretical mass–radius relation and observations from white dwarfs in binary systems. In particular, we find a thin hydrogen mass of $M_{\mathrm{H}} \sim 2 \times 10^{-8}\,\mathrm{M}_{\odot}$ for 40 Eridani B, in agreement with previous determinations. For Sirius B, the spectroscopic mass is 4.3 per cent lower than the dynamical mass. However, the values of mass and radius from gravitational redshift observations are compatible with the theoretical mass–radius relation for a thick hydrogen envelope of $M_{\mathrm{H}} = 2 \times 10^{-6}\,\mathrm{M}_{\odot}$.

Key words: binaries: general – stars: interiors – white dwarfs.

1 INTRODUCTION

One of the results of Chandrasekhar's theory for the structure of white dwarf stars is a dependence of the radius on the stellar mass, known as the mass–radius relation. This relation is widely used in stellar astrophysics. It makes it possible to estimate the stellar mass of white dwarf stars from spectroscopic temperatures and gravities, which in turn are used to determine the mass distribution (see e.g. Koester, Schulz & Weidemann 1979; Bergeron, Leggett & Ruiz 2001; Liebert et al. 2005; Falcon et al. 2012; Holberg, Oswalt & Barstow 2012; Tremblay et al. 2017). In addition, a determination of the white dwarf mass distribution contains information about the star formation history and is directly related to the initial–final mass function (Catalán et al. 2008; Cummings et al. 2016; El-Badry, Rix & Weisz 2018), which determines how much stellar material is returned to the interstellar medium, affecting the chemical evolution of the Galaxy.

Semi-empirical determinations of the mass–radius relations can be obtained from atmospheric parameters, effective temperature, and surface gravity, which combined with flux measurements and parallax can lead to a determination of the radius and stellar mass (Provencal et al. 1998; Holberg et al. 2012; Bédard, Bergeron & Fontaine 2017). This technique started with the works by Schmidt (1996) and Vauclair et al. (1997), who used atmospheric parameters and trigonometric parallax measurements for 20 white dwarfs observed with the *Hipparcos* satellite. Later, this technique was expanded to include wide binary systems for which the primary has a precise parallax from *Hipparcos* (Provencal et al. 1998; Holberg et al. 2012) and *Gaia* DR1 (Tremblay et al. 2017). However, this method is not completely independent of theoretical models, since the determination of the radius depends on the flux emitted at the surface of the star, which is based on the predictions of model atmospheres. In addition, the determinations of the effective temperature and surface gravity also rely on model atmospheres, usually through spectral fitting, which can suffer from large uncertainties, up to ∼0.1 in log g and 1–

★ E-mail: alejandra.romero@ufrgs.br

© 2019 The Author(s)
Published by Oxford University Press on behalf of the Royal Astronomical Society

10 per cent in temperature (Joyce et al. 2018a; Tremblay et al. 2019).

For eclipsing binary systems, the mass and radius of the white dwarf component can be obtained from photometric observations of the eclipses and kinematic parameters, without relying on white dwarf model atmospheres, except for the determination of the effective temperature. However, the specific configuration of eclipsing binaries implies that they have most probably interacted in the past, as common-envelope binaries (Tremblay et al. 2017). A sample of eclipsing binaries containing a white dwarf component applied to the study of the mass–radius relation can be found in Parsons et al. (2010, 2012a,b, 2017). In particular, Parsons et al. (2017) analysed a sample of 16 white dwarfs in detached eclipsing binaries and estimated their mass and radius up to a precision of 1–2 per cent.

Another method to test the mass–radius relation is to rely on astrometric binaries with precise orbital parameters, in particular a dynamical mass determination and distances. Examples of those systems are Sirius, 40 Eridani, and Procyon, for which recent determinations of the dynamical masses based on detailed orbital parameters were reported by Bond et al. (2017a), Mason, Hartkopf & Miles (2017), and Bond et al. (2015), respectively. However, the radius of the white dwarf component cannot be determined from orbital parameters and other techniques are necessary to estimate this parameter. In particular, for the systems mentioned above, the radius is estimated from the measured flux and precise parallax, depending on model atmospheres.

From evolutionary model computations for single stars, it is known that the theoretical mass–radius relation depends systematically on the effective temperature, core composition, helium abundance, and hydrogen abundance in the case of DA white dwarf stars (Wood 1995; Fontaine, Brassard & Bergeron 2001; Renedo et al. 2010; Salaris et al. 2010; Romero, Campos & Kepler 2015). Previous theoretical mass–radius relations (e.g. Wood 1995; Fontaine et al. 2001) have assumed a constant hydrogen layer thickness, which is applied to all models regardless of progenitor and white dwarf mass, typically being $M_{\rm H}/M_* = 10^{-4}$ (Iben & Tutukov 1984). However, full evolutionary computations from Romero et al. (2012, 2013) showed that the upper limit for the mass of the hydrogen layer in a DA white dwarf depends on the total mass of the remnant. The hydrogen content can vary from $M_{\rm H}/M_* \sim 10^{-3}$, for white dwarf masses of $\sim$0.5 $M_\odot$, to $M_{\rm H}/M_* = 10^{-6}$ for massive white dwarfs with $\sim$1 $M_\odot$. In addition, asteroseismological studies show strong evidence of the existence of a hydrogen layer mass range in DA white dwarfs, within the range $10^{-9.5} < M_{\rm H}/M_* < 10^{-4}$, with an average of $M_{\rm H}/M_* \sim 10^{-6.3}$ (Fontaine & Brassard 2008; Castanheira & Kepler 2009; Romero et al. 2012). The mass of the hydrogen layer is an important factor, since the mass–radius relation varies by 1–15 per cent, depending on the white dwarf mass and temperature, if a thick ($10^{-4}M_*$) or a thin ($10^{-10}M_*$) hydrogen layer is assumed (Tremblay et al. 2017).

In this work, we study the dependence of the mass–radius relation on the mass of the hydrogen layer. The white dwarf cooling sequences employed are those from Romero et al. (2012, 2013, 2017), extracted from the full evolutionary computations using the LPCODE evolutionary code (Althaus et al. 2005; Renedo et al. 2010). The model grid expands from $\sim$0.493 $M_\odot$ to 1.05 $M_\odot$ in white dwarf mass, where carbon–oxygen core white dwarfs are found. We also consider a range in hydrogen envelope mass from $\sim 10^{-3}M_*$ to $\sim 5 \times 10^{-10}M_*$, depending on the stellar mass.

We compare our theoretical sequences with mass and radius determinations for white dwarfs in binary systems, in order to test the predictions of the theoretical mass–radius relation and to measure the hydrogen content in the star, when possible. We consider four white dwarfs in astrometric binaries – 40 Eridani B (Mason et al. 2017), Sirius B (Bond et al. 2017a), Procyon B (Bond et al. 2015), and Stein 2051 B (Sahu et al. 2017) – and a sample of 11 white dwarfs in detached eclipsing binaries (Parsons et al. 2017).

The paper is organized as follows. In Section 2 we briefly describe the evolutionary cooling sequences used in our analysis. Section 3 is devoted to study the evolution of the hydrogen mass in the white dwarf cooling sequence for different stellar masses. In Section 4 we present an analysis of the dependence of the total radius of the white dwarf on the hydrogen envelope mass and the possible impact on the spectroscopic stellar mass determinations. We also compare our theoretical cooling sequences with other model grids used in the literature. Section 5 is devoted to presenting the comparison between our theoretical models and the mass and radius obtained for white dwarfs in binary systems. Final remarks are presented in Section 6.

2 COMPUTATIONAL DETAILS

2.1 Input physics

The white dwarf cooling sequences employed in this work are those from Romero et al. (2012, 2013, 2017), extracted from full evolutionary computations calculated with the LPCODE evolutionary code. Details on the code can be found in Althaus et al. (2005, 2010), Rened et al. (2010), and Romero et al. (2015). LPCODE computes the evolution of single stars with low and intermediate mass at the main sequence, starting at the zero-age main sequence, going through the hydrogen- and helium-burning stages, the thermally pulsing and mass-loss stages on the asymptotic giant branch (AGB), to the white dwarf cooling evolution. Here we briefly mention the main input physics relevant for this work.

The LPCODE evolutionary code considers a simultaneous treatment of non-instantaneous mixing and burning of elements (Althaus et al. 2003). The nuclear network accounts explicitly for 16 elements and 34 nuclear reactions, which include *pp* chain, CNO cycle, helium burning, and carbon ignition (Renedo et al. 2010).

We consider the occurrence of extra-mixing beyond each convective boundary following the prescription of Herwig et al. (1997), except for the thermally pulsing AGB phase. We treated the extra-mixing as a time-dependent diffusion process, assuming that the mixing velocities decay exponentially beyond each convective boundary. The diffusion coefficient is given by $D_{\rm EM} = D_0 {\rm exp}(-2z/fH_{\rm P})$, where $H_{\rm P}$ is the pressure scale height at the convective boundary, D_0 is the diffusion coefficient of unstable regions close to the convective boundary, z is the geometric distance from the edge of the convective boundary, and f describes the efficiency and was set to $f = 0.016$ (see Romero et al. 2015 for details). Mass-loss episodes follow the prescription from Schröder & Cuntz (2005) during the core helium burning and the red giant branch phases, and the prescription of Vassiliadis & Wood (1993) during the AGB and thermally pulsating AGB phases (De Gerónimo et al. 2017, 2018). During the white dwarf evolution, we considered the distinct physical processes that modify the inner chemical profile. In particular, element diffusion strongly affects the chemical composition profile throughout the outer layers. Indeed, our sequences develop a pure hydrogen envelope with increasing thickness as evolution proceeds. Our treatment of time-dependent diffusion is based on the multicomponent gas treatment presented in Burgers (1969). We consider gravitational settling and thermal and chemical

Downloaded from https://academic.oup.com/mnras/article-abstract/484/2/2711/5289881 by Iowa State University user on 05 February 2019

diffusion of H, ^{3}He, ^{4}He, ^{12}C, ^{13}C, ^{14}N, and ^{16}O (Althaus et al. 2003). To account for the convection process in the interior of the star, we adopted the mixing length theory, in its ML2 flavour, with the free parameter $\alpha = 1.61$ (Tassoul, Fontaine & Winget 1990) during the evolution previous to the white dwarf cooling curve and $\alpha = 1$ during the white dwarf evolution. Last, we considered the chemical rehomogenization of the inner carbon–oxygen profile induced by Rayleigh–Taylor instabilities following Salaris et al. (1997).

For the white dwarf stage, the input physics of the code includes the equation of state of Segretain et al. (1994) for the high-density regime complemented with an updated version of the equation of state of Magni & Mazzitelli (1979) for the low-density regime. Other physical ingredients considered in LPCODE are the radiative opacities from the OPAL opacity project (Iglesias & Rogers 1996) supplemented at low temperatures with the molecular opacities of Alexander & Ferguson (1994). Conductive opacities are those from Cassisi et al. (2007), and the neutrino emission rates are taken from Itoh et al. (1996) and Haft, Raffelt & Weiss (1994).

Cool white dwarf stars are expected to crystallize as a result of strong Coulomb interactions in their very dense interior (van Horn 1968). In the process, two additional energy sources, i.e. the release of latent heat and the release of gravitational energy associated with changes in the chemical composition of the carbon–oxygen profile induced by crystallization (Garcia-Berro et al. 1988; Winget et al. 2009), are considered self-consistently and locally coupled to the full set of equations of stellar evolution. The chemical redistribution due to phase separation has been considered following the procedure described in Montgomery & Winget (1999) and Salaris et al. (1997). To assess the enhancement of oxygen in the crystallized core, we used the azeotropic-type formulation of Horowitz, Schneider & Berry (2010).

2.2 Model grid

The DA white dwarf cooling sequences considered in this work are the result of full evolutionary computations of progenitor stars with stellar masses between 0.95 and 6.6 $\mathrm{M}_\odot$ at the zero-age main sequence. The initial metallicity was set to $Z = 0.01$. As a result, the stellar mass range in the cooling sequence expands from $\sim$0.493 M to 1.05 $M_\odot$, where carbon-oxygen core white dwarfs are found. These sequences were presented in the works of Renedo et al. (2010); Romero et al. (2012, 2013, 2017). The values of stellar mass of our model grid are listed in Table 1, along with the hydrogen and helium content as predicted by single stellar evolution, for an effective temperature of $\sim$12 000 K. The central abundance of carbon and oxygen for each mass is also listed. Note that the value of the hydrogen content listed in Table 1 is the maximum possible value, since a larger hydrogen mass will trigger nuclear reactions, consuming all the exceeding material (see Section 3). The upper limit for the possible hydrogen content shows a strong dependence on the stellar mass. It ranges from $1.6 \times 10^{-4}\,\mathrm{M}_\odot$ for $M_* = 0.493\,\mathrm{M}_\odot$ to $1.5 \times 10^{-6}\,\mathrm{M}_\odot$ for $M_* = 1.050\,\mathrm{M}_\odot$, with a value $\sim 10^{-4} M_*$ for the averaged-mass sequence of $M_* = 0.60\,\mathrm{M}_\odot$, for effective temperatures near the beginning of the ZZ Ceti instability strip. The helium abundance also shows a dependence on the stellar mass, decreasing monotonically with increase of the stellar mass. In particular, the sequence with $1.05\,\mathrm{M}_\odot$ was obtained by artificially scaling the stellar mass from the $0.976\,\mathrm{M}_\odot$ sequence at high effective temperatures (see Romero et al. 2013 for details). Since no residual helium burning is present in the cooling sequence, the helium content does not change, and both sequences present similar helium content.

Table 1. The main characteristics of our set of DA white dwarf models. The stellar mass at the white dwarf stage is listed in column 1. Also listed are the hydrogen mass at 12 000 K (column 2), the helium mass (column 3), and the central abundances of carbon (column 4) and oxygen (column 5).

$M_\star/\mathrm{M}_\odot$	$-\log(M_\mathrm{H}/M_\star)$	$-\log(M_\mathrm{He}/M_\star)$	X_C	X_O
0.493	3.50	1.08	0.268	0.720
0.525	3.62	1.31	0.278	0.709
0.548	3.74	1.38	0.290	0.697
0.570	3.82	1.46	0.301	0.696
0.593	3.93	1.62	0.283	0.704
0.609	4.02	1.61	0.264	0.723
0.632	4.25	1.76	0.234	0.755
0.660	4.26	1.92	0.258	0.730
0.705	4.45	2.12	0.326	0.661
0.721	4.50	2.14	0.328	0.659
0.770	4.70	2.23	0.332	0.655
0.800	4.84	2.33	0.339	0.648
0.837	5.00	2.50	0.347	0.640
0.878	5.07	2.59	0.367	0.611
0.917	5.41	2.88	0.378	0.609
0.949	5.51	2.92	0.373	0.614
0.976	5.68	2.96	0.374	0.613
0.998	5.70	3.11	0.358	0.629
1.024	5.74	3.25	0.356	0.631
1.050	5.84	2.96	0.374	0.613

Uncertainties related to the physical processes occurring during the AGB stage lead to uncertainties in the amount of hydrogen remaining on the envelope of a white dwarf star. For instance, the hydrogen mass can be reduced to a factor of two as a result of the carbon enrichment of the envelope due to third-dredge-up episodes at the thermally pulsing AGB phase (Althaus et al. 2015). Also, the hydrogen envelope mass depends on the initial metallicity of the progenitor, being a factor of 2 thicker when the metallicity decreases from $Z = 0.01$ to $Z = 0.001$ (Renedo et al. 2010; Romero et al. 2015). However, the mass-loss rate during the AGB and planetary nebula stages will not strongly impact the amount of hydrogen left on the white dwarf (Althaus et al. 2015).

In order to compute cooling sequences with different values of the thickness of the hydrogen envelope, in particular thinner than the value expected by the burning limit, ^{1}H was replaced with ^{4}He at the bottom of the hydrogen envelope (see Romero et al. 2012, 2013 for details). This procedure is done at high effective temperatures ($\gtrsim$90 000 K), so the transitory effects caused by the artificial procedure are quickly washed out. The values of hydrogen content as a function of the stellar mass are depicted in Fig. 1. The thick red line connects the values of the maximum value of M_H predicted by our stellar evolution computations.

3 THE EVOLUTION OF THE HYDROGEN CONTENT

After the end of the Thermally pulsing Asymptotic Giant Branch (TP-AGB) stage, during the post-AGB evolution at nearly constant luminosity, simple models of the white dwarf progenitors show that CNO cycle reactions reduce the hydrogen content below a critical value. If the star has a white dwarf mass of $0.6\,\mathrm{M}_\odot$, the value of the critical hydrogen mass is $\sim 2 \times 10^{-4}\,\mathrm{M}_\odot$ (Iben 1982, 1984; Iben & Renzini 1983). Residual nuclear burning will reduce the hydrogen mass in the surface layers to $\sim 10^{-4}\,\mathrm{M}_\odot$. These values change with

Downloaded from https://academic.oup.com/mnras/article-abstract/484/2/2711/5289881 by Iowa State University user on 05 February 2019

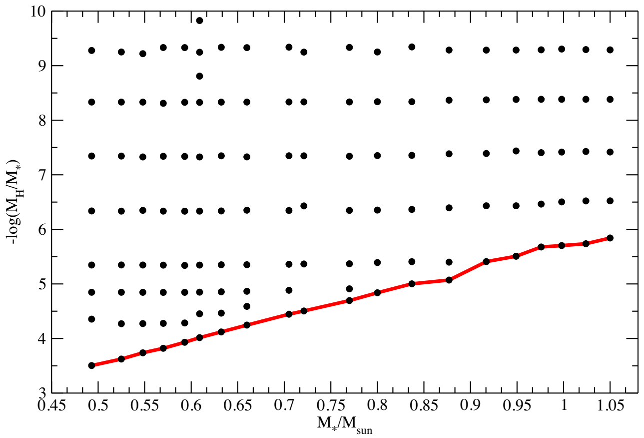

Figure 1. Grid of DA white dwarf evolutionary sequences considered in this work in the $M_*/\mathrm{M}_\odot$ versus $-\log{(M_\mathrm{H}/M_*)}$ plane. Each circle corresponds to a sequence of models representative of white dwarf stars characterized by a given stellar mass and hydrogen envelope mass. The envelope mass is measured at an effective temperature of 12 000 K. The red line connects the sequences with the maximum values for the thickness of the hydrogen envelope, predicted by our evolutionary computations.

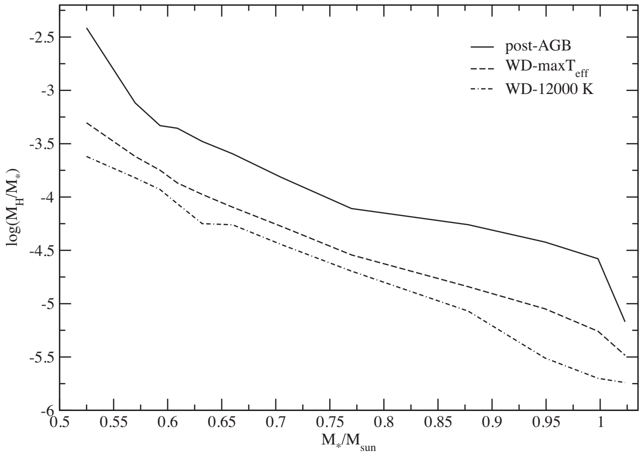

Figure 2. Hydrogen mass as a function of the white dwarf stellar mass for three points during the evolution: during the nearly constant luminosity stage post-AGB at $T_\mathrm{eff} \sim 10\,000$ K (post-AGB), at the point of maximum effective temperature when the star enters the cooling sequence (WD-maxT_eff), and on the cooling curve at $T_\mathrm{eff} \sim 12\,000$ K (WD-12 000 K) evolutionary computations.

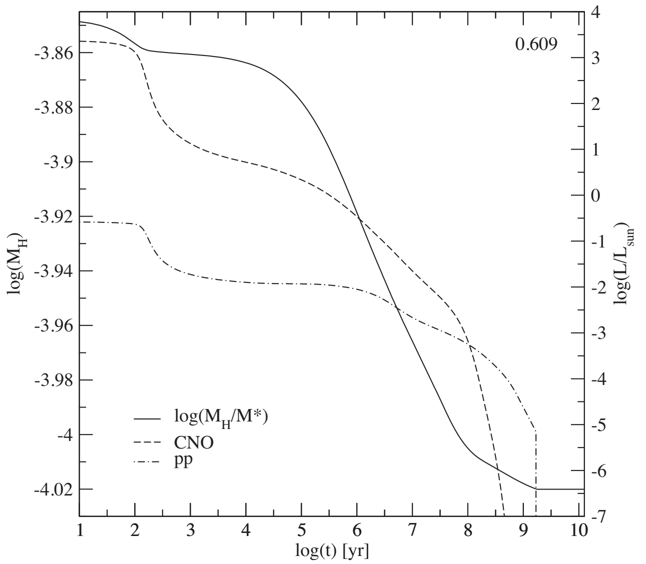

Figure 3. Temporal evolution of the hydrogen content M_H (in units of M_*) and the ratio of hydrogen nuclear burning to surface luminosity for the CNO bi-cycle and *pp* chain, for a white dwarf sequence with stellar mass 0.609 $\mathrm{M}_\odot$. The time corresponds to the cooling time in years measured from the point of maximum effective temperature at the beginning of the cooling curve.

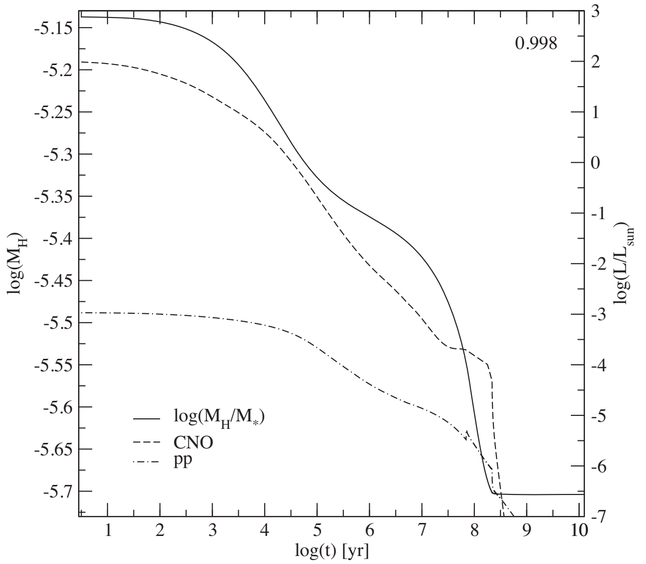

Figure 4. Same as Fig. 3 but for a sequence with stellar mass 0.998 $\mathrm{M}_\odot$. The time corresponds to the cooling time in years.

the white dwarf mass when the evolution previous to and during the cooling curve is computed consistently. In Fig. 2 we show the hydrogen mass as a function of the white dwarf mass for three points during the evolution: the point with $T_\mathrm{eff} \sim 10\,000$ K during the post-AGB stage, previous to the white dwarf phase (solid line); the point of maximum effective temperature when the star enters the cooling curve (dashed line); and at $T_\mathrm{eff} \sim 12\,000$ K on the white dwarf cooling curve (dot–dashed line). As can be seen from Fig. 2, the major reduction of the hydrogen mass occurs during the post-AGB evolution, for all stellar masses, due to CNO shell burning. For a $M_\mathrm{WD} \sim 0.6\,\mathrm{M}_\odot$, the hydrogen content is $\sim 2.8 \times 10^{-4}\,\mathrm{M}_\odot$ at 10 000 K on the post-AGB stage, and it reduces to $\sim 1.1 \times 10^{-4}\,\mathrm{M}_\odot$ when the star enters the white dwarf cooling curve.

Residual burning at the cooling curve can further reduce the hydrogen envelope by a factor of ∼2 (see Fig. 2). Figs 3 and 4 show the temporal evolution of the hydrogen content for sequences with white dwarf stellar mass 0.609 and 0.998 $\mathrm{M}_\odot$, respectively, during the cooling curve. Also shown are the luminosity given by the nuclear burning of hydrogen due to the CNO bi-cycle and the *pp* chain as a function of the logarithm of the cooling time in years, measured from the point of maximum effective temperature when the star enters the white dwarf cooling curve. As can be seen, the hydrogen burning is reducing the hydrogen envelope mass during the early evolutionary phases of the white dwarf stage. At the beginning of the cooling sequence, the 0.609 $\mathrm{M}_\odot$ sequence has a hydrogen content of $M_H/\mathrm{M}_\odot = 8.6 \times 10^{-5}$, which

Downloaded from https://academic.oup.com/mnras/article-abstract/484/2/2711/5289881 by Iowa State University user on 05 February 2019

is reduced due to residual hydrogen burning to a constant value of $M_H/\mathrm{M}_{\odot} = 5.8 \times 10^{-5}$ after 1.76 Gyr. As can be seen from Fig. 3, the CNO bi-cycle dominates the energy production due to hydrogen burning for the first ∼110 Myr of the cooling sequences. Hydrogen burning due to the *pp* chain lasts longer, causing a small reduction in the hydrogen content of the model. Once the hydrogen content decreases below a certain threshold, the pressure at the bottom of the envelope is not large enough to support further nuclear reactions. After no residual nuclear burning is present in the star, the main energy source of the white dwarf is the release of gravothermal energy. A similar scenario is found for the more massive sequence shown in Fig. 4. The star enters the cooling sequence with a hydrogen content of $M_H/\mathrm{M}_{\odot} = 7.3 \times 10^{-6}$, 10 times smaller than the hydrogen content in the 0.609 $\mathrm{M}_{\odot}$ model at the same stage. After 580 Myr, the hydrogen content reaches a somewhat constant value of $M_H/\mathrm{M}_{\odot} = 1.97 \times 10^{-6}$. In this case, because of the higher temperature at the base of the envelope, the contribution to the energy production from the CNO bi-cycle is five orders of magnitude larger than the contribution from the proton–proton chain at the beginning of the cooling sequence, it being the dominant source while residual nuclear reactions are still active.

3.1 Massive white dwarf with ‘thick’ hydrogen envelope

The hydrogen content in the envelope of a white dwarf can increase due to accretion from a companion star. Depending on the distance to the companion, a certain amount of mass can be added on top of the white dwarf. However, if the hydrogen content exceeds the limiting value for nuclear reactions, the H shell at the bottom of the hydrogen envelope can be activated and the additional hydrogen is consumed, leading to an equilibrium mass. To explore this scenario, we computed the cooling evolution of a 1 $\mathrm{M}_{\odot}$ white dwarf sequence with a thick hydrogen layer. To simulate the accreted material, we artificially increased the hydrogen envelope mass at high effective temperatures, near the beginning of the cooling sequence. For a white dwarf with 1 $\mathrm{M}_{\odot}$, the remaining hydrogen content predicted by single stellar evolution is $M_{\mathrm{H}}/M_* = 2.1 \times 10^{-6}$ (see Table 1). Thus, we increased the hydrogen mass to a factor 100, $M_{\mathrm{H}}/M_* = 10^{-4}$, and computed the following evolution considering possible sources of nuclear burning. Fig. 5 shows the evolution in the H–R diagram for this sequence. The colour bar indicates the hydrogen envelope mass in a logarithmic scale. As expected, the hydrogen burning shell at the bottom of the hydrogen envelope is active again, consuming the excess in the hydrogen content. The residual burning makes the model move to the high-luminosity and low-temperature region of the H–R diagram, similar to what happens in the low-mass regime that produces pre-Extremelly low mass white dwarf stars (Althaus, Miller Bertolami & Córsico 2013; Istrate, Tauris & Langer 2014). Once the hydrogen content is reduced below the limiting value for nuclear burning, the star settles on to the cooling sequence one more time with a hydrogen mass of $\sim 2.5 \times 10^{-6} M_*$, similar to the value obtained from single evolution computations. Therefore, the final hydrogen content would not change significantly due to accretion.

4 RADIUS AND HYDROGEN CONTENT

As it was mentioned, the mass–radius relation depends on the amount of hydrogen and helium present in the star. In particular, the hydrogen envelope, although it contains a very small amount of mass, appears to be the dominant parameter in the determination of the radius for DA white dwarfs (Tremblay et al. 2017). Thus, a reduction of the hydrogen, and/or helium content, will lead to a smaller radius and thus to an increase in the surface gravity. This effect is depicted in Fig. 6, where we show white dwarf evolutionary sequences in the $\log g$–T_{eff} plane for stellar masses from 0.493 to 0.998 $\mathrm{M}_{\odot}$. The black line indicates the sequence with the thickest hydrogen envelope, as predicted by single stellar evolution. As expected, the surface gravity increases when the hydrogen content decreases for a given stellar mass at a given

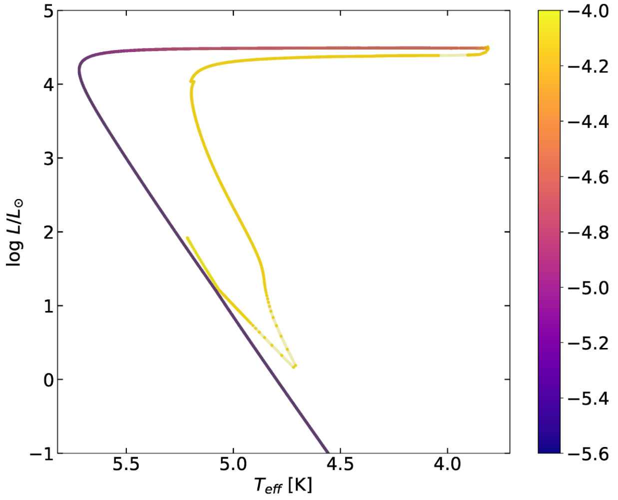

Figure 5. Evolution in the H–R diagram for a sequence of 1 $\mathrm{M}_{\odot}$ in the white dwarf cooling sequence with an artificially increased hydrogen envelope of $M_{\mathrm{H}} \sim 10^{-4} M_*$ at the beginning of the cooling curve. This scenario simulates the possible accretion of material due to interaction with a binary companion. The colour bar indicates the amount of hydrogen left in the envelope of the star. Note that if residual thermonuclear burning is considered, the amount of hydrogen decreases and reaches a value of $\sim 2.5 \times 10^{-6} M_*$, similar to that obtained from single stellar evolution.

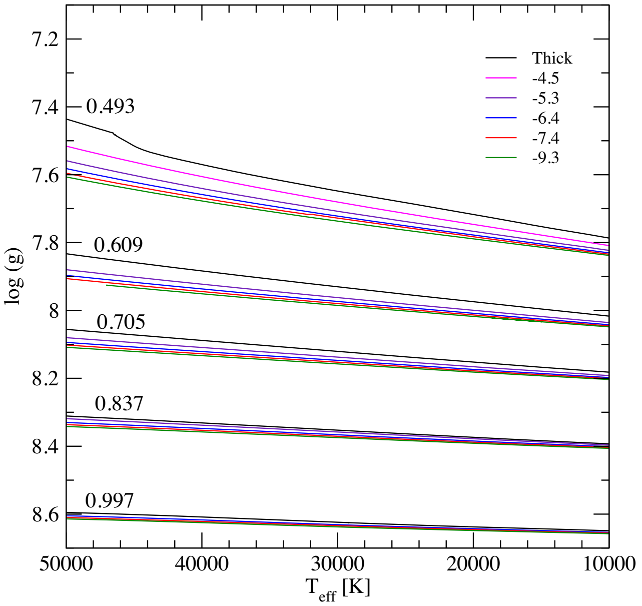

Figure 6. Cooling tracks for different hydrogen envelopes in the T_{eff} – $\log g$ plane. The thickness of the hydrogen envelope decreases from top to bottom, and it is labelled in the figure in $\log (M_{\mathrm{H}}/M_*)$. The stellar mass for each group of sequences is indicated.

Downloaded from https://academic.oup.com/mnras/article-abstract/484/2/2711/5289881 by Iowa State University user on 05 February 2019

Table 2. Radius (in $R_\odot$) and surface gravity (g in cm s^{-2}) extracted from theoretical cooling sequences, for 40 000 K (columns 2 and 3) and 20 000 K (columns 4 and 5), for the stellar masses presented in Fig. 6.

0.493	R (40 kK)	log g	R (20 kK)	log g
Thick	0.019137	7.5683	0.016157	7.7153
−5.3	0.017661	7.6380	0.015266	7.7646
−6.4	0.017222	7.6586	0.014986	7.7793
−7.4	0.017017	7.6690	0.014927	7.7828
−9.3	0.016826	7.6788	0.014814	7.7894
0.609	R (40 kK)	log g	R (20 kK)	log g
Thick	0.014794	7.8825	0.013306	7.9747
−5.3	0.014181	7.9206	0.012982	7.9973
−6.4	0.013899	7.9368	0.012796	8.0086
−7.4	0.013766	7.9451	0.012723	8.0136
−9.3	0.013658	7.9520	0.012662	8.0177
0.705	R (40 kK)	log g	R (20 kK)	log g
Thick	0.0125432	8.0891	0.0116590	8.1526
−5.3	0.0122555	8.1093	0.0114827	8.1658
−6.4	0.0120894	8.1211	0.0113798	8.1737
−7.4	0.0120037	8.1273	0.0113274	8.1777
−9.3	0.0119206	8.1334	0.0112778	8.1815
0.837	R (40 kK)	log g	R (20kK)	log g
Thick	0.0103397	8.3315	0.0098452	8.3744
−5.3	0.0110280	8.3365	0.0098002	8.3781
−6.4	0.0101528	8.3474	0.0097275	8.3846
−7.4	0.0100880	8.3530	0.0096864	8.3882
−9.3	0.0100311	8.3579	0.0096513	8.3914
0.998	R (40 kK)	log g	R (20 kK)	log g
Thick	0.008221	8.6082	0.007945	8.6377
−6.4	0.008124	8.6172	0.007886	8.6430
−7.4	0.008084	8.6215	0.007860	8.6458
−9.3	0.008050	8.6251	0.007837	8.6484

temperature. The effect is less important for higher stellar masses, since they form with thinner hydrogen envelopes. For instance, the maximum mass for the hydrogen content in a 0.998 $M_\odot$ sequence is 100 times thinner than that corresponding to a 0.6 $M_\odot$ sequence (see Table 1 for details). The radius and log g for the stellar masses are listed in Table 2 for effective temperatures of 40 000 and 20 000 K.

Comparing the results for the sequences with the thickest envelope with those having the thinnest hydrogen envelope of the grid, the reduction in the total radius is between 8 and 12 per cent for a stellar mass of 0.493 $M_\odot$, 5–8 per cent for stellar mass 0.609 $M_\odot$, and almost negligible, 1–2 per cent, for a model with 0.998 $M_\odot$, within the ranges of hydrogen mass considered in this work. However, this reduction in the total radius has a strong impact on the surface gravity value, specially for high effective temperatures, being 0.11, 0.08, and 0.02 dex in log g for stellar masses 0.493, 0.609, and 0.998 $M_\odot$, respectively, for $T_{\rm eff} = 40\,000$ K. For an effective temperature of 20 000 K, the increase in log g is 0.08, 0.07, and 0.011 dex, respectively. Considering that the real mean uncertainty from spectroscopic fits in log g is ∼0.038 dex (Barstow et al. 2005; Liebert et al. 2005), it is possible to estimate the hydrogen layer for stellar masses lower than ∼0.7 $M_\odot$, but not for higher stellar masses, unless the uncertainties are reduced to less than 0.011 dex in log g.

4.1 Comparison with other theoretical models

In the literature, we can find a few grids of theoretical white dwarf cooling sequences. Wood (1995) computed DA white dwarf cooling sequences to study the white dwarf luminosity function of our Galaxy. He considered a stratified model with various central compositions, from pure C to pure O. The computations start as polytropes and the early evolution is characterized by a contraction phase at a constant luminosity of $\sim 10^2\,L_\odot$, before entering the cooling curve (Winget et al. 1987). The growing degeneracy in the core halts the contraction and the surface temperature reaches a maximum of $T_{\rm eff} \geq 100\,000$ K. In particular, the models presented in Wood (1995) have a fixed hydrogen content of $\sim 10^{-4} M_*$.

Another widely used set of white dwarf sequences is that computed by the Montreal group,[1] and published in Fontaine et al. (2001). The first set of models for DA white dwarfs had a C pure core and a helium and hydrogen content of $10^{-2} M_*$ and $10^{-4} M_*$, respectively, for sequences with stellar mass in the range between 0.2 and 1.3 $M_\odot$. Latter, additional models with a C/O = 50/50 were computed with a helium content $10^{-2} M_*$ and two different values for the hydrogen mass, $10^{-4} M_*$ (‘thick’) and $10^{-10} M_*$ (‘thin’).

Finally, Salaris et al. (2010) presented a set of white dwarf cooling sequences with stellar masses between 0.54 and 1 $M_\odot$. For each white dwarf mass, an initial model was converged at $L \sim 10^2\,L_\odot$, considering a chemical composition profile taken from pre-white-dwarf computations, specifically at the first thermal pulse (Salaris et al. 2000). The hydrogen and helium mass are set to $M_{\rm H} = 10^{-4} M_*$ and $M_{\rm He} = 10^{-2} M_*$, respectively, for all stellar masses, as in Fontaine et al. (2001).

In all cases, the authors assume a constant thickness of the hydrogen layer for all stellar masses. In order to keep the hydrogen mass at a strictly constant value, no residual thermonuclear burning has been included in the calculations. In particular, Salaris et al. (2010) stated that H burning at the bottom of the hydrogen envelope is negligible in all but the more massive models. In addition, the cooling sequences presented in those works do not compute the post-AGB and planetary nebula stages, crucial to determine the hydrogen envelope mass at the white dwarf stage.

As we show in Section 2.2, the maximum mass of hydrogen left on top of a white dwarf model depends on the stellar mass. In particular, the hydrogen envelope mass is larger than $10^{-4} M_*$ for stellar masses lower than ∼0.6 $M_\odot$, while sequences with white dwarf masses larger than ∼0.6 $M_\odot$ show thinner hydrogen envelopes, with masses below $10^{-4} M_*$. The extension of the hydrogen envelope will impact the total radius of the star and consequently the value of log g. For instance, the hydrogen envelope mass for a ∼1 $M_\odot$ white dwarf model is $\sim 10^{-6} M_*$, 100 times thinner than the fixed value considered in previous works, leading to a ∼5 per cent decrease in the stellar radius for those stellar masses and radii.

In Fig. 7, we compare our canonical sequences, those with the thickest hydrogen envelope obtained from single stellar evolution, to the theoretical cooling sequences from Fontaine et al. (2001) with $M_{\rm H} = 10^{-4} M_*$, in the $T_{\rm eff}$–log g plane. Similar results are found when we compare them to the cooling sequences from Wood (1995) and Salaris et al. (2010). To match the stellar mass values from Fontaine et al. (2001), we interpolated the cooling sequences within our model grid. Note that for a stellar mass 0.6 $M_\odot$ the model computed with LPCODE perfectly overlaps with the model computed by Fontaine et al. (2001). This is a consequence of the value of

---

[1] http://www.astro.umontreal.ca/∼bergeron/CoolingModels/

Downloaded from https://academic.oup.com/mnras/article-abstract/484/2/2711/5289881 by Iowa State University user on 05 February 2019

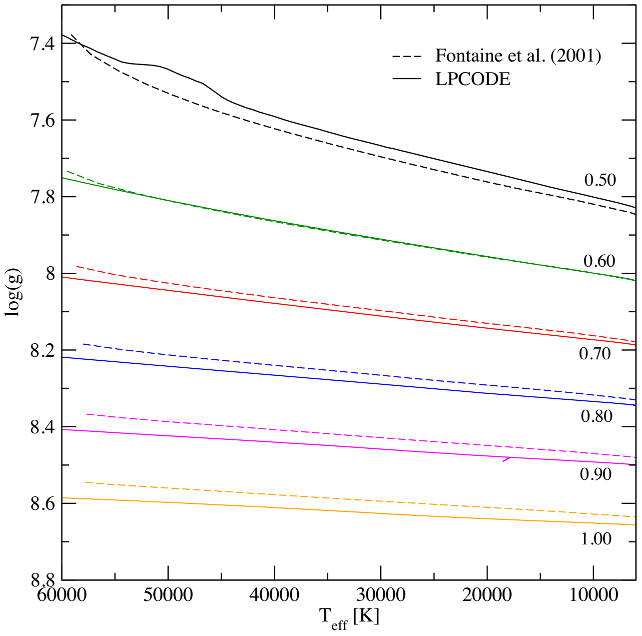

Figure 7. Comparison in the $T_{\rm eff}$ –log g plane of the theoretical cooling sequences computed with LPCODE (solid lines) and those extracted from Fontaine et al. (2001) with $M_{\rm H} = 10^{-4} M_*$ (dashed lines). The labels indicate the stellar mass of the sequences. In order to match the stellar mass values from Fontaine et al. (2001), we interpolated the cooling sequences within our model grid (see Table 1).

the hydrogen envelope mass, which for this stellar mass is nearly $\sim 10^{-4} M_*$ in both cases. For stellar masses below 0.6 $M_\odot$, in this case 0.5 $M_\odot$, the cooling sequence computed with LPCODE shows a lower log g – larger radius – than that from Fontaine et al. (2001), while the opposite happens for sequences with stellar masses larger than 0.6 $M_\odot$. Thus, models with fixed hydrogen envelopes that do not consider the pre-white-dwarf evolution and/or the residual burning sources at the cooling sequence can lead to overestimated or underestimated spectroscopic masses.

5 MEASURING THE HYDROGEN MASS

In this section, we estimate the hydrogen mass content of a selected sample of white dwarf stars in binary systems. The mass and radius for the objects considered in our analysis were taken from the literature and were estimated using different techniques, which are in principle independent of the theoretical mass–radius relation. First we consider two well-studied members of astrometric binary systems, 40 Eridani B and Sirius B. Additionally, we consider two non-DA white dwarfs, Procyon B and Stein 2051 B. Finally, we analyse the results obtained from a sample of 11 detached eclipsing binaries. We do not consider the data fully based on spectroscopic techniques since the uncertainties in the atmospheric parameters, specially in log g, are too large to estimate the hydrogen envelope mass (Joyce et al. 2018a). In each case, we analyse the results and the uncertainties and how they impact the determination of the hydrogen layer mass.

5.1 Astrometric binaries

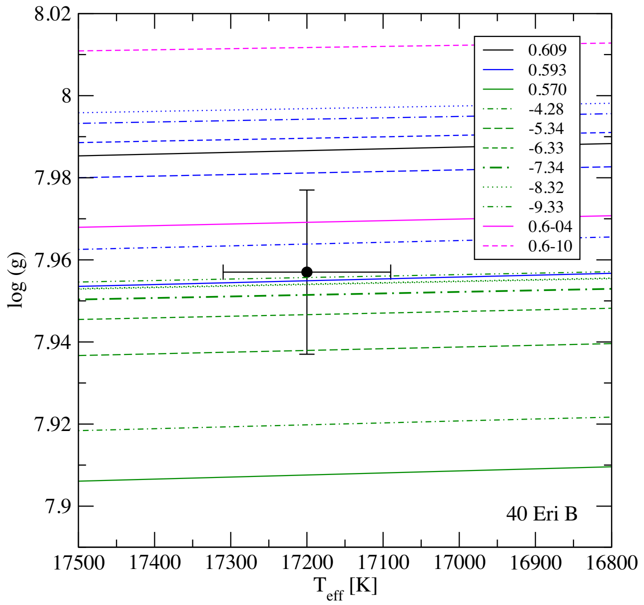

Figure 8. Location of 40 Eridani B in the $T_{\rm eff}$–log g plane. Solid lines correspond to thick envelope sequences, those with the larger amount of hydrogen allowed by single stellar evolution. Thinner envelopes are depicted with different lines (see inset in the figure). The labels associated with the sequences with different thin envelopes correspond to the value of log (M_H/M_*). Different colours indicate different stellar masses (in solar units). The green and blue lines correspond to sequences with 0.570 and 0.593 $M_\odot$, respectively, while the black solid line corresponds to a sequence with 0.609 $M_\odot$. The magenta lines correspond to sequences from Fontaine et al. (2001) for a stellar mass 0.6 $M_\odot$ with thick (0.6–04) and thin (0.6–10) hydrogen envelopes.

Astrometric binaries are an important tool to test the mass–radius relation, since independent determinations of the stellar mass can be obtained from the dynamical parameters of the binary system and accurate distances. The determination of the radius, on the other hand, is not model-independent, since it depends on the value of the flux emitted at the surface itself. We consider that, for these systems, the dynamical parameters and distances are precise enough to set constrains not only on the theoretical mass–radius relation but also on the hydrogen content. In this section, we use the observational determinations of mass and radius for four white dwarfs in astrometric binary systems.

5.1.1 40 Eridani B

40 Eridani B was for many years reported as a low-mass white dwarf with a stellar mass of ~ 0.4 $M_\odot$. Recently, Mason et al. (2017) determined a dynamical mass of 0.573 ± 0.018 $M_\odot$ using observations of the orbit covering a longer period of time and the updated *Hipparcos* parallax. Later, Bond, Bergeron & Bédard (2017b) determined the atmospheric parameters of this star using spectroscopy and obtained an effective temperature of 17 200 ± 110 K and a surface gravity of log g = 7.957 ± 0.020. In addition, these authors determined the radius of 40 Eridani B using photometric observations combined with the distance (see Bédard et al. 2017 for details), it being $R = 0.01308 \pm 0.00020$ $R_\odot$.

From the spectroscopic parameters derived by Bond et al. (2017b), we computed the stellar mass for 40 Eridani B from evolutionary tracks in the $T_{\rm ef}$–log g plane for different values of the hydrogen envelope thickness. In Fig. 8 we depict the location of 40 Eridani B along with theoretical white dwarf cooling tracks com-

Downloaded from https://academic.oup.com/mnras/article-abstract/484/2/2711/5289881 by Iowa State University user on 05 February 2019

puted with LPCODE, with different hydrogen envelope thicknesses ranging from $10^{-4}M_*$ to $2 \times 10^{-10}M_*$ and stellar mass between 0.570 and 0.609 $M_\odot$. We also plotted two cooling sequences from Fontaine et al. (2001) with 0.6 $M_\odot$ for thick ($10^{-4}M_*$) and thin ($10^{-10}M_*$) hydrogen envelopes.

If we consider the uncertainties in the atmospheric parameters, specifically in $\log g$, the stellar mass varies when the different hydrogen envelope thicknesses are taken into account (Tremblay et al. 2017). From Fig. 8, we note that the spectroscopic stellar mass is higher if we consider thick envelope tracks, those with the thickest hydrogen envelope allowed by our models of single stellar evolution, and it decreases for thinner hydrogen envelopes. We computed the stellar mass for each envelope thickness. The results are listed in Table 3, along with the corresponding hydrogen mass in solar units and the determinations of the dynamical mass (Shipman et al. 1997; Mason et al. 2017) and the spectroscopic mass (Bond et al. 2017b). We notice that the spectroscopic stellar mass varies from 0.594$M_\odot$, for the thick-envelope set of tracks, to 0.571 $M_\odot$, ~4 per cent lower, for the thinnest value. Note that the values for the spectroscopic mass for the two thinnest envelopes are the same, implying that this parameter is not sensitive to the hydrogen envelope once it is thinner than 2.79×10^{-9} $M_\odot$. The spectroscopic mass that better matches the value of the dynamical mass from Mason et al. (2017) is the one characterized by a hydrogen envelope of $M_H = 2.63 \times 10^{-8}$ $M_\odot$. If we consider 1σ uncertainties, the hydrogen mass is between $M_H = 2.63 \times 10^{-6}$ $M_\odot$ and $M_H = 2.67 \times 10^{-10}$ $M_\odot$. Thus, we conclude that the hydrogen envelope for 40 Eridani B should be thinner than the value predicted by single stellar evolution. This result is consistent with previous works (Holberg et al. 2012; Bédard et al. 2017; Bond et al. 2017b). In particular, Bond et al. (2017b) found a spectroscopic mass somewhat lower than the values presented in this work, but they also found a thin envelope for 40 Eridani B, consistent with $fM_H = 10^{-10}$ $M_\odot$.

Another way to estimate the hydrogen mass in 40 Eridani B is by comparing the radius and dynamical mass to the theoretical mass–radius relation. This is shown in Fig. 9, where we depict the mass–radius relations for six different envelope thicknesses. The solid black curve corresponds to the mass–radius relation for thick-envelope sequences. The thinnest hydrogen envelope in the model grid is $\log (M_H/M_*) \sim -9.33$. From Fig. 9, we see that the observations of 40 Eridani B are in agreement with a thin-envelope solution. Specifically, the upper limit for the hydrogen mass is the same as the one obtained using the value of the dynamical mass and the spectroscopic parameters (Fig. 8).

The cooling age for 40 Eridani B, for a stellar mass of (0.573 ± 0.0011) $M_\odot$, is ~145 Myr. Considering the initial-to-final mass relation from Romero et al. (2015) for solar metallicity, we estimate a progenitor mass of 1.53 ± 0.11 $M_\odot$ and a total age of 2.68 ± 0.43 Gyr for 40 Eridani B.

5.1.2 *Sirius B*

Sirius B is the brightest and nearest of all white dwarfs, located at 2.65 pc. Combining the information from the orbital parameters and parallax, Bond et al. (2017a) determined a dynamical mass of $M_B = 1.018 \pm 0.011$ $M_\odot$ for Sirius B. In addition, Bond et al. (2017a) reported spectroscopic atmospheric parameters of $T_{\rm eff} = 25\,369 \pm 46$ K and $\log g = 8.591 \pm 0.016$ and a radius of $R = 0.008098 \pm 0.000046$ $R_\odot$. Note that the surface gravity calculated from the radius and dynamical mass is $\log g = 8.629 \pm 0.007$, not compatible with the spectroscopic value within 2σ (Bond et al. 2017a). More recently, Joyce et al. (2018b) determined the mass for Sirius B using the effect of gravitational redshift and a radius from the flux and the parallax, and obtained values of $M_* = 1.017 \pm 0.025$ $M_\odot$ and $R_* = 0.00803 \pm 0.00011$ $R_\odot$, in agreement with those of Bond et al. (2017a).

Using the spectroscopic parameters reported in Bond et al. (2017a), we proceed to estimate the stellar mass of Sirius B. In Fig. 10, we depict the location of Sirius B in the $T_{\rm eff}$–$\log g$ plane. Cooling tracks for stellar masses in the range of 0.949–1.024 $M_\odot$ are colour-coded for each stellar mass and the values are indicated for each group. The solid lines correspond to thick-envelope sequences, while thinner envelopes, i.e. with $M_H/M_* < 2 \times 10^{-6}$, are depicted with different lines, with increasing $\log g$ when M_H decreases. The figure includes cooling curves with 1 $M_\odot$ from Fontaine et al. (2001). The spectroscopic mass, determined using our evolutionary tracks, results in ~0.974 $M_\odot$ for the sequences with the thickest envelope, 4.3 per cent lower than the dynamical mass, in agreement with previous determinations of the spectroscopic mass (Barstow et al. 2005; Holberg et al. 2012; Bédard et al. 2017; Joyce et al. 2018a). The spectroscopic stellar mass for each hydrogen envelope mass, computed using the LPCODE cooling tracks, is listed in Table 3. Also listed are stellar mass determinations from observations.

Also from Fig. 10, while the cooling track from Fontaine et al. (2001) for a thin hydrogen envelope (1.0-10) overlaps with the cooling sequences of LPCODE with the same mass, the track with a thick hydrogen envelope (1.0-04, 10^{-4}) overlaps with the LPCODE tracks with a stellar mass of 0.973 $M_\odot$. We can easily explain the difference in $\log g$ with the different total hydrogen mass in the models, since, for our models, the thickest hydrogen envelope mass for a ~1 $M_\odot$ white dwarf is $\sim 2 \times 10^{-6}M_*$, two orders of magnitude thinner than the value adopted by Fontaine et al. (2001) (see Section 4.1). We compute an additional sequence with 0.988 $M_\odot$ and a thick hydrogen envelope of $\sim 10^{-4}M_*$, labelled as '0998-Thick' in Fig. 10. We used the same technique described in Section 3.1, but we turned off all hydrogen nuclear reactions to keep its hydrogen content fixed. Note that with a hydrogen envelope ~100 times more massive, our model with 0.998 $M_\odot$ is able to nearly reproduce the spectroscopic surface gravity for Sirius B. Although the hydrogen content is the dominant factor, additional discrepancies in the surface gravities between the thick-envelope models can be explained with the difference in the helium content, being arbitrarily set to $10^{-2}M_*$ for the models from Fontaine et al. (2001) and being set by stellar evolution to $10^{-3.1}M_*$ for the models computed with LPCODE.

Note that the uncertainties associated with the spectroscopic determinations of the atmospheric parameters in the literature correspond to internal errors and could be as large as 1.2 per cent in effective temperature and 0.038 dex in $\log g$ (Barstow et al. 2005; Liebert et al. 2005). In the case of Sirius B, Joyce et al. (2018a) computed the atmospheric parameters using different spectra for *HST* and found a dispersion for $\log g$ of 0.05 dex, leading to spectroscopic stellar masses between 0.874 and 0.962 $M_\odot$. With this criterion, the uncertainties in the spectroscopic mass are 3 times larger than the ones considered by Bond et al. (2017a). In addition, the uncertainties presented by Bond et al. (2017a) correspond to uncorrelated internal uncertainties of the fitting, even though the orbital parameters and stellar masses are correlated. By computing the uncertainties using a simple error propagation statistic, we obtain an uncertainty ~48 per cent larger for the mass of Sirius B, implying that the quoted uncertainties could be underestimated.

Downloaded from https://academic.oup.com/mnras/article-abstract/484/2/2711/5289881 by Iowa State University user on 05 February 2019

Table 3. Stellar mass determinations for different hydrogen envelope layers, considering the spectroscopic atmospheric parameters for 40 Eridani B (left) and Sirius B (right). Also listed are the dynamical mass (Mason et al. 2017) and the spectroscopic mass derived by Bond et al. (2017b). Dynamical masses and other spectroscopic determinations are listed in the last three rows.

$M_H/\mathrm{M}_\odot$	Mass ($\mathrm{M}_\odot$)	$M_H/\mathrm{M}_\odot$	Mass ($\mathrm{M}_\odot$)
6.87×10^{-5}	0.594 ± 0.010		
3.07×10^{-5}	0.589 ± 0.010		
2.64×10^{-6}	0.580 ± 0.010	2.02×10^{-6}	0.974 ± 0.013
2.67×10^{-7}	0.575 ± 0.010	3.16×10^{-7}	0.970 ± 0.015
2.63×10^{-8}	0.573 ± 0.011	3.66×10^{-8}	0.968 ± 0.014
2.79×10^{-9}	0.571 ± 0.011	4.00×10^{-9}	0.967 ± 0.014
2.65×10^{-10}	0.571 ± 0.011	4.87×10^{-10}	0.966 ± 0.014
Shipman et al. (1997)(1)	0.501 ± 0.011	Bond et al. (2017a)(1)	1.018 ± 0.011
Mason et al. (2017)(1)	0.573 ± 0.018	Barstow et al. (2005)(2)	0.978 ± 0.005
Bond et al. (2017b)(2)	0.565 ± 0.031	Joyce et al. (2018b)(3)	1.017 ± 0.025

Note. Values of the stellar mass determined by the techniques: (1)dynamical mass, (2)fully spectroscopical, and (3)gravitational redshift.

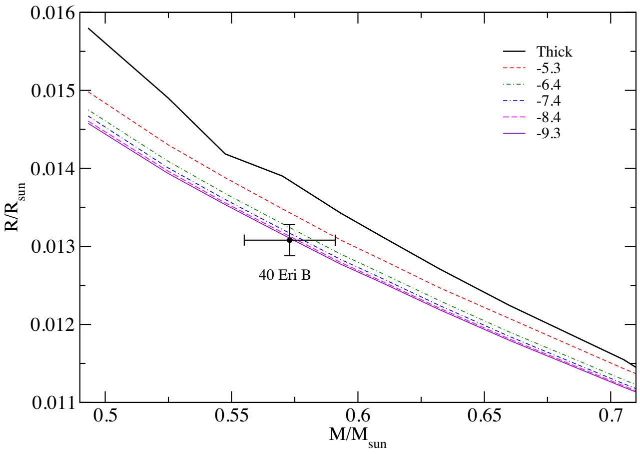

Figure 9. Location of 40 Eridani B in the mass–radius plane, where the values correspond to the dynamical mass (Mason et al. 2017) and radius (Bond et al. 2017b). The curves are the mass–radius relation for an effective temperature of $T_{\mathrm{eff}} = 17\,200$ K, corresponding to the spectroscopic temperature of 40 Eridani B. Each curve is characterized by a value of M_H/M_*. The black solid line ('Thick') corresponds to the maximum hydrogen content allowed by single stellar evolution.

In Fig. 11 we compare the observational parameters for Sirius B with our theoretical models using the mass–radius relation. The different lines correspond to theoretical mass–radius relations for an effective temperature of $T_{\mathrm{eff}} = 25\,369$ K. The solid black line corresponds to the sequences with the thickest hydrogen envelope allowed by single stellar evolution, computed with LPCODE, while the solid magenta line corresponds to the thinnest envelope, with $M_{\mathrm{H}} \sim 10^{-9.33} M_*$. We also show the theoretical mass–radius relation from Fontaine et al. (2001) with hydrogen envelope mass $M_{\mathrm{H}} \sim 10^{-4} M_*$ as a dashed line. We include the gravitational redshift mass from Joyce et al. (2018b) obtained using parallaxes from *Hipparcos* (full triangle) and *Gaia* DR2 (open triangle), from Bond et al. (2017a) (full square), and from Barstow et al. (2005) (red diamond). With a black circle, we show the result obtained by considering the spectroscopic mass computed in this work combined with the radius from Joyce et al. (2018b).

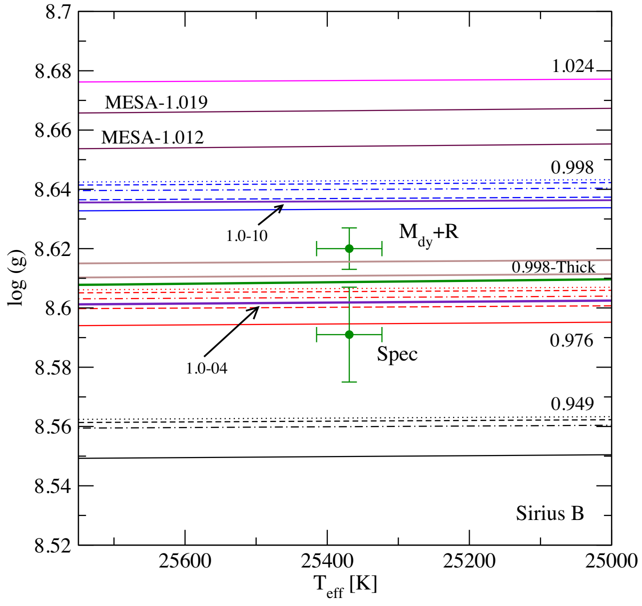

Figure 10. Location of Sirius B in the T_{eff}–$\log g$ plane, using the spectroscopic determinations (Spec) and the dynamical mass combined with the radius ($M_{\mathrm{dy}} + R$) from Bond et al. (2017a). The lines correspond to theoretical white dwarf sequences, which are colour-coded in stellar mass: black lines for 0.949 $\mathrm{M}_\odot$, red lines for 0.976 $\mathrm{M}_\odot$, blue lines for 0.998 $\mathrm{M}_\odot$, and magenta lines for 1.024 $\mathrm{M}_\odot$. Solid lines correspond to canonical sequences. Thinner envelopes are depicted with different lines, being thinner as $\log g$ increases. The violet lines correspond to the cooling tracks from Fontaine et al. (2001) for a stellar mass of 1.0 $\mathrm{M}_\odot$ with thick (1.0–04) and thin (1.0–10) hydrogen envelopes. Just for comparison, we included two tracks computed with the MESA code with stellar masses 1.012 and 1.019 $\mathrm{M}_\odot$ from Lauffer, Romero & Kepler (2018). The thick brown line labelled '0.998-Thick' corresponds to a cooling track computed with LPCODE having thicker hydrogen envelopes than the canonical value (see text for details).

As expected, the spectroscopic mass and the dynamical mass from Bond et al. (2017a) do not agree within the uncertainties in 1σ. However, the results from Joyce et al. (2018b) are compatible with our theoretical mass–radius relation, within 1σ for a hydrogen envelope with $M_{\mathrm{H}} \sim 2 \times 10^{-6} M_*$. Note that the mass and radius

Downloaded from https://academic.oup.com/mnras/article-abstract/484/2/2711/5289881 by Iowa State University user on 05 February 2019

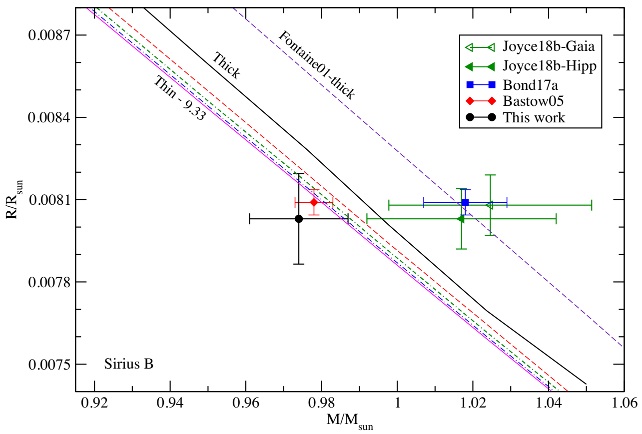

Figure 11. Same as Fig. 9 but for Sirius B and an effective temperature of $T_{\rm eff} = 25\,369$ K. The points show the location of the spectroscopic mass obtained in this work combined with the radius from Joyce et al. (2018b) (circle), the dynamical mass from Bond et al. (2017a) (square), and the gravitational redshift mass from Joyce et al. (2018b) considering parallax from *Hipparcos* (full triangle) and *Gaia* DR2 (open triangle).

for Sirius B from Joyce et al. (2018b) are also in agreement with the 'thick' envelope, with $M_{\rm H} = 10^{-4} M_*$, sequences from Fontaine et al. (2001).

A thicker envelope could perhaps be expected if Sirius B had accretion episodes after the residual nuclear burning had turned off. Considering that the Sirius system is a visual binary with a period of ~50 yr (Bond et al. 2017a), this scenario can be disregarded. The accretion rate of hydrogen from the interstellar medium is less than $10^{-17}\,{\rm M}_\odot\,{\rm yr}^{-1}$ (Dupuis et al. 1993; Koester & Kepler 2015), too low to build a thick hydrogen envelope of $\sim 10^{-4} M_*$. In any case, as it was shown in Section 3.1, the increase of the hydrogen content will trigger nuclear burning at the base of the envelope, reducing the hydrogen mass to $\sim 10^{-6} M_*$.

Davis et al. (2011) determined the structure parameters for Sirius A using photometry and spectroscopy combined with parallax to be $R = 1.7144 \pm 0.009\,{\rm R}_\odot$, $T = 9845 \pm 64$ K, and $L = 24.74 \pm 0.70\,{\rm L}_\odot$. Considering the uncertainties in mass and metallicity, we estimate an age between 205 and 245 Myr. With a cooling age of 115 ± 6 Myr, the stellar mass of the progenitor of Sirius B is $5.11^{+0.47}_{-0.28}\,{\rm M}_\odot$, in agreement with the value obtained by Bond et al. (2017a) and Liebert et al. (2005).

5.1.3 Binaries with non-DA white dwarf components

In this section, we briefly consider two non-DA white dwarfs in binary systems: Procyon B and Stein 2051 B. Procyon B is a DQZ white dwarf with an effective temperature of 7740 ± 50 K (Provencal et al. 2002) in a binary system with a slightly evolved subgiant of spectral type F5 IV–V. The Procyon system was analysed by Bond et al. (2015) using precise relative astrometry for *HST* observations combined with ground-base observations and parallax. For Procyon B, the dynamical mass resulted in $M_* = 0.593 \pm 0.006\,M_\odot$ and the radius, determined using flux and parallax measurements, was $0.01232 \pm 0.00032\,{\rm R}_\odot$.

Stein 2051 B is a DC white dwarf with $T_{\rm eff} = 7122 \pm 181$ K, in a binary system with a main-sequence companion of spectral type M4. The stellar mass was determined by Sahu et al. (2017) using astrometric microlensing, $M = 0.75 \pm 0.051\,{\rm M}_\odot$, while the radius of $R_* = 0.0114 \pm 0.0004\,{\rm R}_\odot$ was determined using photometry and parallax measurements.

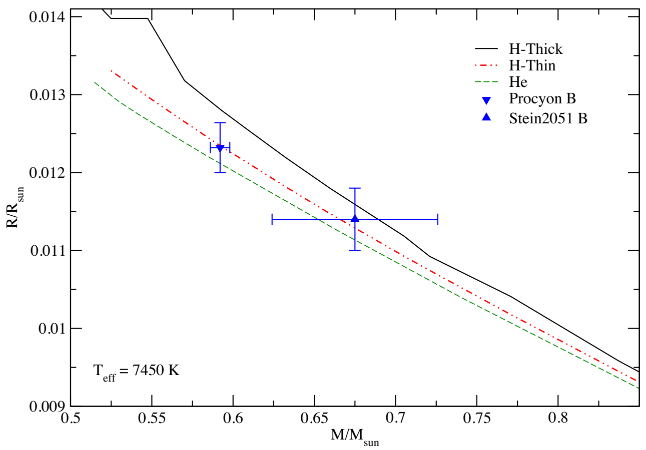

Figure 12. Same as Fig. 9 but for the non-DA white dwarfs Procyon B and Stein 2051 B, where the observations are those from Bond et al. (2015) and Sahu et al. (2017), respectively. The curves are the mass–radius relation for an effective temperature $T_{\rm eff} = 7450$ K, for thick (solid black line) and thin ($M_{\rm H} = 10^{-9} M_*$, red point–dashed line) and DB white dwarf models from Althaus et al. (2009) (green dashed line).

Fig. 12 shows the position of Procyon B and Stein 2051 B as compared to the theoretical mass–radius relations for $T_{\rm eff} = 7450$ K. The red point-dashed line corresponds to thin hydrogen envelope models, with $M_{\rm H} = 10^{-9} M_*$ while the green dashed line corresponds to DB white dwarf models from Althaus et al. (2009). We also included the mass–radius relation for thick envelope models computed with LPCODE, those with the thickest hydrogen envelope allowed by stellar evolution. Considering the uncertainties reported by Bond et al. (2015), Procyon B is in very good agreement with our theoretical models for thin H envelope, as it was found by Bond et al. (2015, 2017b), but is also in agreement with the theoretical mass–radius relation for DB white dwarfs. The results for Stein 2051 B are not that conclusive since the uncertainties are too large, but are still consistent with the theoretical models.

5.2 Eclipsing binaries

Parsons et al. (2017) presented mass and radius determinations for 16 white dwarfs in detached eclipsing binaries with low-mass main-sequence star companions and combined them with 10 previous measurements to test the theoretical mass–radius relation. The mass and radius are estimated from the eclipses and radial velocity measurements, while the effective temperature of the white dwarf component is determined using spectroscopy. We selected the objects with stellar masses larger than $\sim 0.5\,{\rm M}_\odot$ that are covered by our model grid. The selected sample is depicted in Fig. 13, where we compare the observations extracted from Parsons et al. (2017) to the theoretical mass–radius relation. The solid (dashed) lines correspond to the theoretical mass–radius relations for canonical ($M_{\rm H}/{\rm M}_\odot = 10^{-10}$) models for effective temperatures from 60 000 K to 10 000 K, from top to bottom, in steps of 10 000 K (see figure for details). From this figure, we see a very good agreement between models and observations, being also consistent in effective temperature.

Downloaded from https://academic.oup.com/mnras/article-abstract/484/2/2711/5289881 by Iowa State University user on 05 February 2019

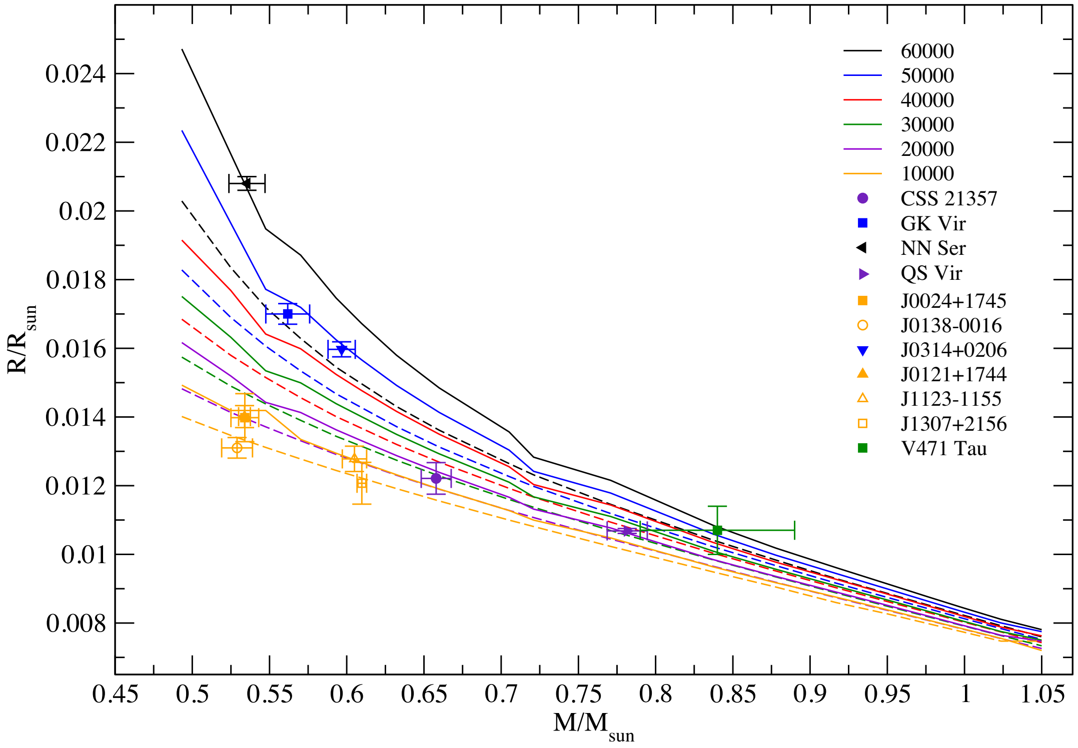

Figure 13. The white dwarf mass–radius relation. Solid lines correspond to thick-envelope models, while dashed lines correspond to sequences with $M_H/M_* = 10^{-10}$. From top to bottom, the solid lines are colour-coded, corresponding to effective temperatures of 60 000 (black), 50 000 (blue), 40 000 (red), 30 000 (green), 20 000 (violet), and 10 000 K (orange). The data points are the sample extracted from Parsons et al. (2017) and are indicated with different symbols that are colour-coded as well.

Next we proceed to measure the hydrogen content in the selected sample of 11 white dwarfs. The sample is listed in Table 4, along with the effective temperature, stellar mass, and radius extracted from Parsons et al. (2017). For each object, we compare the observed mass and radius with our theoretical mass–radius relation, considering different thicknesses of the hydrogen envelope. From the selected sample, only five objects, GK Vir, NN Ser, J0138−0016, J0121+1744, and J1123−1155, show uncertainties small enough to measure the hydrogen envelope mass, within our model grid. The remaining objects are consistent with the theoretical mass–radius relation but the uncertainties are too large to constrain the mass of the hydrogen content. The results for the five objects are depicted in Fig. 14, while the values for the hydrogen envelopes are listed in the last column of Table 4. From Fig. 14, it shows that all five objects have a canonical hydrogen envelope, i.e. the maximum amount of hydrogen as predicted by stellar evolution theory. This is expected given the mass range of the objects, for which the hydrogen envelope is intrinsically thicker. Also, note that the larger differences between the theoretical mass–radius relations for different hydrogen envelope masses occur for low stellar masses and higher effective temperatures, as shown in Fig. 6.

6 CONCLUSIONS

In this work, we studied the mass–radius relation for white dwarf stars and its dependence on the hydrogen envelope mass, in particular, how the extension of the hydrogen envelope affects the radius, and the surface gravity, which directly impacts the calculation of the stellar mass using atmospheric parameters, i.e. the spectroscopic mass.

We find that, comparing the sequences with the thickest envelope with those having the thinnest hydrogen envelope in our model grid, the reduction in the radius is around 8–12 per cent, 5–8 per cent, and 1–2 per cent for stellar masses of 0.493, 0.609, and 0.998 $M_\odot$, respectively. As expected, the differences are larger for models with a lower stellar mass since, for these objects, the maximum hydrogen envelope left on top of a white dwarf star is thicker, according to single stellar evolution theory. The reduction of the stellar radius translates directly to an increase in $\log g$ for a fixed stellar mass, which can reach up to 0.11 dex, for low mass and high effective temperatures. Considering that the mean uncertainty in $\log g$ is 0.038 dex, then it is possible to measure the hydrogen envelope mass.

In addition, the maximum hydrogen mass allowed by stellar evolution theory is mass dependent, being thinner than $M_{\rm H} = 10^{-4} M_*$, for white dwarf masses larger than 0.6 $M_\odot$, and thicker for masses below 0.6 $M_\odot$. Thus, considering a hydrogen envelope of $M_{\rm H} = 10^{-4} M_*$ for all stellar masses can lead to overestimated or underestimated spectroscopic masses.

The hydrogen envelope mass is the dominant factor influencing the value of the radius. The central composition leads to a less than 1 per cent difference in the radius, as shown by Tremblay et al. (2017). For the helium content, the radius can be reduced by ~1.1 per cent if the helium mass is reduced by more than a factor of 10.

We also use the mass–radius relation as a tool to measure the mass of the hydrogen envelope. We analyse a sample of white dwarfs in astrometric and eclipsing binaries, for which it is possible to determine the mass and radius independently of the theoretical

Downloaded from https://academic.oup.com/mnras/article-abstract/484/2/2711/5289881 by Iowa State University user on 05 February 2019

Table 4. White dwarf stars in detached eclipsing binaries analysed in Fig. 14. For each object, we list the effective temperature, stellar mass, and radius (columns 2, 3, and 4) from Parsons et al. (2017) and the hydrogen envelope mass determined in this work.

Obj ID	$T_{\rm eff}$ (K)	M ($\mathrm{M}_\odot$)	R ($\mathrm{R}_\odot$)	M_H/M_*
CSS 21357	15909 ± 285	0.6579 ± 0.0097	0.01221 ± 0.00046	$5.8 \times 10^{-5} - 4.6 \times 10^{-10}$
GK Vir	50000 ± 673	0.5618 ± 0.0142	0.01700 ± 0.00030	$(1.67 \pm 0.30) \times 10^{-4}$
NN Ser	63000 ± 3000	0.5354 ± 0.0117	0.02080 ± 0.00020	$(2.18 \pm 0.23) \times 10^{-4}$
QS Vir	14220 ± 350	0.7816 ± 0.0130	0.01068 ± 0.00007	$1.8 \times 10^{-5} - 4.6 \times 10^{-10}$
J0024+1745	8272 ± 580	0.5340 ± 0.0090	0.01398 ± 0.00070	$2.2 \times 10^{-4} - 2.6 \times 10^{-10}$
J0138−0016	3570 ± 100	0.5290 ± 0.0100	0.01310 ± 0.00030	$2.3 \times 10^{-4} - 5.8 \times 10^{-10}$
J0314+0206	46783 ± 7706	0.5967 ± 0.0088	0.01597 ± 0.00022	$(1.25 \pm 0.01) \times 10^{-4}$
J0121+1744	10644 ± 1721	0.5338 ± 0.0038	0.01401 ± 0.00032	$(2.21 \pm 0.73) \times 10^{-4}$
J1123−1155	10210 ± 87	0.6050 ± 0.0079	0.01278 ± 0.00037	$(1.02 \pm 0.10) \times 10^{-4}$
J1307+2156	8500 ± 500	0.6098 ± 0.0031	0.01207 ± 0.00061	$9.6 \times 10^{-5} - 1.4 \times 10^{-10}$
V471 Tau	34500 ± 1000	0.8400 ± 0.0500	0.01070 ± 0.00070	$9.8 \times 10^{-6} - 4.8 \times 10^{-10}$

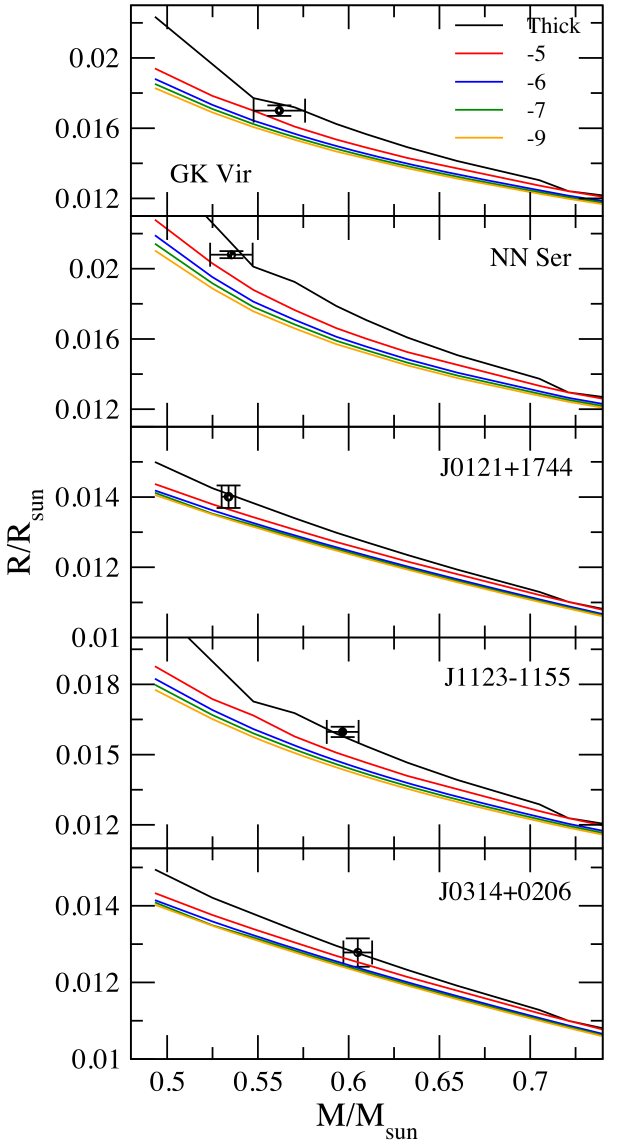

Figure 14. Comparison with the observational values for mass and radius for five white dwarfs in eclipsing binaries presented in Parsons et al. (2017), with the theoretical mass–radius relations for different masses of the hydrogen envelope. Each panel corresponds to a single object. The hydrogen envelope for each curve is colour-coded (see inset in the figure).

models. We consider 4 white dwarfs in astrometric binaries with very well-determined orbital parameters and a sample of 11 white dwarf stars in detached eclipsing binary systems. Our main results are the following.

(i) For 40 Eridani B, we find a spectroscopic mass of $(0.573 \pm 0.0011)\,\mathrm{M}_\odot$ and a hydrogen envelope mass of $M_{\rm H} \sim 2.63 \times 10^{-8}\,\mathrm{M}_\odot$. This result is in agreement with previous determinations, pointing to a thin hydrogen envelope solution. The cooling age for 40 Eridani B is ∼145 Myr, with a total age of 2.68 ± 0.43 Gyr and a progenitor mass of $1.53 \pm 0.11\,\mathrm{M}_\odot$.

(ii) For Sirius B, we find a spectroscopic stellar mass of $(0.974 \pm 0.013)\,\mathrm{M}_\odot$, in agreement with previous determinations (Barstow et al. 2005). In addition, the gravitational redshift mass from Joyce et al. (2018b), as compared with our theoretical mass–radius relation, is in agreement within 1σ, considering a thick hydrogen envelope of $M_{\rm H} = 2.02 \times 10^{-6}$. The cooling age for Sirius B is 115 ± 6 Myr, leading to a stellar mass of the progenitor of $5.11^{+0.47}_{-0.28}\,\mathrm{M}_\odot$. As compared to the dynamical mass, the spectroscopic value is 4.3 per cent lower than that obtained by Bond et al. (2017a), and not compatible within the uncertainties. We conclude that either the uncertainties in the dynamical mass are underestimated by at least ∼ 50 per cent or the difference is due to the fitting method and/or current atmospheric models.

(iii) Observations of both non-DA white dwarfs, Procyon B and Stein 2051 B, are consistent with a thin hydrogen envelope ($M_{\rm H} \lesssim 10^{-9}$) as found by Bond et al. (2017b), but also with the pure He theoretical models from Althaus et al. (2009).

(iv) For a sample of 11 white dwarfs in detached eclipsing binaries we found a good agreement between the theoretical mass–radius relation and the observations. For five objects, in the low-mass range ($\lesssim 0.6\,\mathrm{M}_\odot$), we measured the hydrogen mass and found thick hydrogen envelopes in all cases. For the remaining objects, the uncertainties are too large to constrain the hydrogen envelope mass, but the observations are in agreement with the theoretical mass–radius relation.

In general, the mass–radius relation computed using our models is in good agreement with the observations. For some objects, we were able to constrain the hydrogen envelope mass given the lower uncertainties in the observed mass and radius. However, for most objects uncertainties are still too large. High-mass white dwarf models show that these stars are born with hydrogen envelopes

Downloaded from https://academic.oup.com/mnras/article-abstract/484/2/2711/5289881 by Iowa State University user on 05 February 2019

of $\sim 10^{-6} M_*$ or thinner. Thus, the challenge of constraining the hydrogen mass is higher since the difference in radius is 1–2 per cent within the hydrogen mass range allowed by our model grid.

Finally, we emphasize that the maximum hydrogen content left on top of a white dwarf is mass dependent, when the evolution of the white dwarf progenitor is computed consistently. In particular, the hydrogen envelope is thinner than the canonical value for stellar masses larger than $0.6\,\mathrm{M}_\odot$ and thicker for stellar masses below that value. Not taking into account this dependence can lead to a overestimation of the stellar mass when the determination is based on spectroscopy, i.e. using the atmospheric parameters $\log g$ and effective temperature.

ACKNOWLEDGEMENTS

We thank our anonymous referee for the constructive comments and suggestions. ADR, SOK, and GRL had financial support from CNPq and PRONEX-FAPERGS/CNPq (Brazil). SRGJ acknowledges support from the Science and Technology Facilities Council (STFC, UK). AHC had financial support by AGENCIA through the Programa de Modernización Tecnológica BID 1728/OC-AR, and by the PIP 112-200801-00940 grant from CONICET. Special thanks to Leandro Althaus for computing the model described in Fig. 5 and for the very useful comments on the manuscript. This research has made use of the NASA Astrophysics Data System.

REFERENCES

Alexander D. R., Ferguson J. W., 1994, ApJ, 437, 879
Althaus L. G., Serenelli A. M., Córsico A. H., Montgomery M. H., 2003, A&A, 404, 593
Althaus L. G., Serenelli A. M., Panei J. A., Córsico A. H., García-Berro E., Scóccola C. G., 2005, A&A, 435, 631
Althaus L. G., Panei J. A., Miller Bertolami M. M., García-Berro E., Córsico A. H., Romero A. D., Kepler S. O., Rohrmann R. D., 2009, ApJ, 704, 1605
Althaus L. G., Córsico A. H., Bischoff-Kim A., Romero A. D., Renedo I., García-Berro E., Miller Bertolami M. M., 2010, ApJ, 717, 897
Althaus L. G., Miller Bertolami M. M., Córsico A. H., 2013, A&A, 557, A19
Althaus L. G., Camisassa M. E., Miller Bertolami M. M., Córsico A. H., García-Berro E., 2015, A&A, 576, A9
Barstow M. A., Bond H. E., Holberg J. B., Burleigh M. R., Hubeny I., Koester D., 2005, MNRAS, 362, 1134
Bédard A., Bergeron P., Fontaine G., 2017, ApJ, 848, 11
Bergeron P., Leggett S. K., Ruiz M. T., 2001, ApJS, 133, 413
Bond H. E. et al., 2015, ApJ, 813, 106
Bond H. E. et al., 2017a, ApJ, 840, 70
Bond H. E., Bergeron P., Bédard A., 2017b, ApJ, 848, 16
Burgers J. M., 1969, Flow Equations for Composite Gases. Academic Press, New York
Cassisi S., Potekhin A. Y., Pietrinferni A., Catelan M., Salaris M., 2007, ApJ, 661, 1094
Castanheira B. G., Kepler S. O., 2009, MNRAS, 396, 1709
Catalán S., Isern J., García-Berro E., Ribas I., 2008, MNRAS, 387, 1693
Cummings J. D., Kalirai J. S., Tremblay P.-E., Ramirez-Ruiz E., 2016, ApJ, 818, 84
Davis J., Ireland M. J., North J. R., Robertson J. G., Tango W. J., Tuthill P. G., 2011, PASA, 28, 58
De Gerónimo F. C., Althaus L. G., Córsico A. H., Romero A. D., Kepler S. O., 2017, A&A, 599, A21
De Gerónimo F. C., Althaus L. G., Córsico A. H., Romero A. D., Kepler S. O., 2018, A&A, 613, A46
Dupuis J., Fontaine G., Pelletier C., Wesemael F., 1993, ApJS, 84, 73
El-Badry K., Rix H.-W., Weisz D. R., 2018, ApJ, 860, L17
Falcon R. E., Winget D. E., Montgomery M. H., Williams K. A., 2012, ApJ, 757, 116
Fontaine G., Brassard P., 2008, PASP, 120, 1043
Fontaine G., Brassard P., Bergeron P., 2001, PASP, 113, 409
Garcia-Berro E., Hernanz M., Isern J., Mochkovitch R., 1988, Nature, 333, 642
Haft M., Raffelt G., Weiss A., 1994, ApJ, 425, 222
Herwig F., Bloecker T., Schoenberner D., El Eid M., 1997, A&A, 324, L81
Holberg J. B., Oswalt T. D., Barstow M. A., 2012, AJ, 143, 68
Horowitz C. J., Schneider A. S., Berry D. K., 2010, Phys. Rev. Lett., 104, 231101
Iben I. Jr, 1982, ApJ, 260, 821
Iben I. Jr, 1984, ApJ, 277, 333
Iben I. Jr, Renzini A., 1983, ARA&A, 21, 271
Iben I. Jr, Tutukov A. V., 1984, ApJ, 282, 615
Iglesias C. A., Rogers F. J., 1996, ApJ, 464, 943
Istrate A. G., Tauris T. M., Langer N., 2014, A&A, 571, A45
Itoh N., Hayashi H., Nishikawa A., Kohyama Y., 1996, ApJS, 102, 411
Joyce S. R. G., Barstow M. A., Casewell S. L., Burleigh M. R., Holberg J. B., Bond J. E., 2018a, MNRAS, 479, 1612
Joyce S. R. G., Barstow M. A., Holberg J. B., Bond H. E., Casewell S. L., Burleigh M. R., 2018b, MNRAS, 481, 2361
Koester D., Kepler S. O., 2015, A&A, 583, A86
Koester D., Schulz H., Weidemann V., 1979, A&A, 76, 262
Lauffer G. R., Romero A. D., Kepler S. O., 2018, MNRAS, 480, 1547
Liebert J., Young P. A., Arnett D., Holberg J. B., Williams K. A., 2005, ApJ, 630, L69
Magni G., Mazzitelli I., 1979, A&A, 72, 134
Mason B. D., Hartkopf W. I., Miles K. N., 2017, AJ, 154, 200
Montgomery M. H., Winget D. E., 1999, ApJ, 526, 976
Parsons S. G., Marsh T. R., Copperwheat C. M., Dhillon V. S., Littlefair S. P., Gänsicke B. T., Hickman R., 2010, MNRAS, 402, 2591
Parsons S. G. et al., 2012a, MNRAS, 426, 1950
Parsons S. G. et al., 2012b, MNRAS, 420, 3281
Parsons S. G. et al., 2017, MNRAS, 470, 4473
Provencal J. L., Shipman H. L., Høg E., Thejll P., 1998, ApJ, 494, 759
Provencal J. L., Shipman H. L., Koester D., Wesemael F., Bergeron P., 2002, ApJ, 568, 324
Renedo I., Althaus L. G., Miller Bertolami M. M., Romero A. D., Córsico A. H., Rohrmann R. D., García-Berro E., 2010, ApJ, 717, 183
Romero A. D., Córsico A. H., Althaus L. G., Kepler S. O., Castanheira B. G., Miller Bertolami M. M., 2012, MNRAS, 420, 1462
Romero A. D., Kepler S. O., Córsico A. H., Althaus L. G., Fraga L., 2013, ApJ, 779, 58
Romero A. D., Campos F., Kepler S. O., 2015, MNRAS, 450, 3708
Romero A. D. et al., 2017, ApJ, 851, 60
Sahu K. C. et al., 2017, Science, 356, 1046
Salaris M., Domínguez I., García-Berro E., Hernanz M., Isern J., Mochkovitch R., 1997, ApJ, 486, 413
Salaris M., García-Berro E., Hernanz M., Isern J., Saumon D., 2000, ApJ, 544, 1036
Salaris M., Cassisi S., Pietrinferni A., Kowalski P. M., Isern J., 2010, ApJ, 716, 1241
Schmidt H., 1996, A&A, 311, 852
Schröder K.-P., Cuntz M., 2005, ApJ, 630, L73
Segretain L., Chabrier G., Hernanz M., Garcia-Berro E., Isern J., Mochkovitch R., 1994, ApJ, 434, 641
Shipman H. L., Provencal J. L., Høg E., Thejll P., 1997, ApJ, 488, L43
Tassoul M., Fontaine G., Winget D. E., 1990, ApJS, 72, 335
Tremblay P.-E. et al., 2017, MNRAS, 465, 2849
Tremblay P.-E., Cukanovaite E., Gentile Fusillo N. P., Cunningham T., Hollands M. A., 2019, MNRAS, 482, 5222
van Horn H. M., 1968, ApJ, 151, 227
Vassiliadis E., Wood P. R., 1993, ApJ, 413, 641

Downloaded from https://academic.oup.com/mnras/article-abstract/484/2/2711/5289881 by Iowa State University user on 05 February 2019

Vauclair G., Schmidt H., Koester D., Allard N., 1997, A&A, 325, 1055
Winget D. E., Hansen C. J., Liebert J., van Horn H. M., Fontaine G., Nather R. E., Kepler S. O., Lamb D. Q., 1987, ApJ, 315, L77
Winget D. E., Kepler S. O., Campos F., Montgomery M. H., Girardi L., Bergeron P., Williams K., 2009, ApJ, 693, L6
Wood M. A., 1995, in Koester D., Werner K., eds, Lecture Notes in Physics, Vol. 443. Springer-Verlag, Berlin, p. 41

This paper has been typeset from a TEX/LATEX file prepared by the author.

Downloaded from https://academic.oup.com/mnras/article-abstract/484/2/2711/5289881 by Iowa State University user on 05 February 2019